Supporting Information

Two-in-one template-assisted construction of hollow phosphide nanotubes for electrochemical energy storage

Leiyun Han [a], Xilong Liu [a], Zheng Cui [a], Yang Chen [a], Zijia Wang [a], Yu Tang [a], Yingjie Hua [b*], Chongtai Wang [b], Haijiao Xie [c], Xudong Zhao [a*], Xiaoyang Liu [a, b*]

[a] State Key Laboratory of Inorganic Synthesis and Preparative Chemistry, College of Chemistry, Jilin University, Changchun, 130012, China

[b] Key Laboratory of Electrochemical Energy Storage and Energy Conversion of Hainan Province, School of Chemistry and Chemical Engineering, Hainan Normal University, Haikou, 571158, China

[c] Hangzhou Yanqu Information Technology Co., Ltd. Xixi Legu Creative Pioneering Park, Hangzhou, 310003, China

* E-mail: liuxy@jlu.edu.cn (XY Liu); 521000hua282@sina.com (YJ Hua)

Table of contents

Experimental section

Chemicals

The chemical reagents used in the experiments were all analytically pure and not further purified. Ammonium molybdate tetrahydrate ($(NH_4)_6Mo_7O_{24}\ 4H_2O$), Nitric acid ($HNO_3$, 65%), Hydrochloric acid (HCl, 38%), Nickel sulphate hexahydrate ($NiSO_4 \cdot 6H_2O$), Ferric chloride hexahydrate ($FeCl_3 \cdot 6H_2O$), Ammonium persulfate ($(NH_4)_2S_2O_8$), Polyvinyl alcohol, and Potassium persulfate ($K_2S_2O_8$) are purchased from Sinopharm Chemical Reagent Co., Ltd. Aniline solution (C_6H_7N), Ammonia solution ($NH_3 \cdot H_2O$), and Sodium hypophosphite monohydrate ($NaH_2PO_2 \cdot H_2O$) were purchased from Shanghai Macklin Biochemical Co., Ltd.

Synthesis of MoO_3 nanorods

MoO_3 nanorods was prepared according to previous works with slight modifications [S1]. The detailed process is as follows: 1.4 g of $(NH_4)_6Mo_7O_{24} \cdot 4H_2O$ was stirred and sonicated in 6.66 mL of 65% HNO_3 and 33.33 mL of deionized water. The mixture was then transferred into a 70 mL Teflon-lined stainless-steel autoclave and heated to 180°C at room temperature for 20 h. When the reaction was finished, the precipitate was collected by centrifugation and washed several times with deionized water and ethanol. Finally, the cleaned precipitate was dried in a vacuum oven at 80°C for 12 h.

Synthesis of PANI@MoO_3 nanorods

PANI@MoO_3 nanorods were prepared by *in-situ* polymerization at room temperature. The process is as follows: the prepared 0.10 g MoO_3 nanorods were added

to 10 mL of deionized water and stirred ultrasonically for 20 min for uniform dispersion. The dispersed milky white solution was added drop by drop to a 10 mL (0.1 mol L^{-1}) HCl solution containing 0.30 mL of aniline monomer and stirred continuously for 20 min to allow complete dispersion. Subsequently, 10 mL (1.0 mol L^{-1}) HCl solution containing 0.18 g $(NH_4)_2S_2O_8$ was added dropwise to the aforementioned dispersion solution with continuous stirring and the pH was adjusted to 1-2 by adding HCl (1.0 mol L^{-1}). With continuous stirring, the milky white dispersion gradually changed to a dark green solution, as displayed in **Figure S2(a-c)**. The reaction time was extended to 4 h after the solution turned dark green. After the reaction, the dark green precipitate was collected by centrifugation, and repeated with deionized water and ethanol. Finally, the precipitate was dried in a vacuum oven at 80°C for 12 h.

Synthesis of $Ni(OH)_2$@PANI hollow nanotubes

$Ni(OH)_2$@PANI hollow nanotubes were prepared by CBD at room temperature. The process is as follows: the prepared PANI@MoO_3 nanorods 0.10 g were dispersed in 25 mL $NiSO_4 \cdot 6H_2O$ solution (1.0 mol L^{-1}) and 20 mL $K_2S_2O_8$ solution (0.125 mol L^{-1}) and sonicated for 20 min. After ultrasonic dispersion, 5 mL $NH_3 \cdot H_2O$ was added under continuous stirring, and the reaction was continued for 2 h. After the reaction, the precipitated product was collected by centrifugation and washed several times with deionized water and ethanol. The treated precipitated product was dried in a vacuum oven at 80°C for 12 h, and the final powder sample was collected and denoted as $Ni(OH)_2$@PANI-1M (1M indicates the concentration of 1.0 mol L^{-1} of $NiSO_4 \cdot 6H_2O$). Similarly, the amount of other reagents and reaction conditions remained unchanged,

and only the concentration of $NiSO_4 \cdot 6H_2O$ was changed to 0.5 and 1.5 mol L^{-1}, denoted as $Ni(OH)_2$@PANI-0.5M and $Ni(OH)_2$@PANI-1.5M, respectively. $Ni(OH)_2$ hollow nanotubes were prepared similarly, the MoO_3 nanorods were used as templates and obtained without the addition of aniline solution in the preparation process. Finally, the preparation of PNAI hollow nanotubes was obtained by sonicating the prepared PANI@MoO_3 nanorods in 20 mL of deionized water under continuous stirring, followed by the addition of 5 mL of ammonia solution for 2 h, without the addition of other reagents.

Synthesis of Ni_2P@PANI hollow nanotubes

The hollow Ni_2P@PANI nanotubes (denoted as PNP) were finally prepared by a low-temperature phosphorization reaction in a tube furnace under a nitrogen atmosphere. The process is as follows: $Ni(OH)_2$@PANI-1M hollow nanotubes of 0.10 g were placed in a ceramic crucible with a cover at one end, and 0.22 g of $NaH_2PO_2 \cdot H_2O$ was placed at the other end of the crucible and covered with a lid. Next, the end of the crucible containing $NaH_2PO_2 \cdot H_2O$ was placed on the upstream side of the tube furnace. The sample was then heated to 300°C for 2 h at room temperature in the tube furnace with a gas collection device at a rate of 3°C/min under nitrogen protection (*notably, the low-temperature phosphorization reaction in this experiment should be covered with a lid in the ceramic crucible, otherwise the product cannot be obtained. Furthermore, the phosphorization process produces the toxic and explosive gas PH_3, which requires additional gas treatment and sealing devices to ensure safety during the experiment*). After the reaction was completed, the final product was

collected after cooling to room temperature and marked as PNP-2.2 (2.2 indicates a 2.2:1 mass ratio of phosphorus source to precursor material). Similarly, the amounts of other reagents and reaction conditions were maintained constant, and the mass ratios of phosphorus source and precursors were changed to 1.2:1 and 3.2:1 and marked as PNP-1.2 and PNP-3.2, respectively. Finally, the blank control Ni_2P hollow nanotubes were prepared in the similar manner as the aforementioned $Ni(OH)_2$ hollow nanotubes as precursors, and the products were obtained under the same conditions of phosphatization.

Synthesis of PANI derived nitrogen-doped carbon nanotubes

PANI derived nitrogen-doped carbon nanotubes (denoted as PNCT) were prepared by removing the MoO_3 template from the PANI@MoO_3 nanorods obtained by *in-situ* polymerization at room temperature as described previously, followed by a high-temperature carbonization reaction in the tube furnace under nitrogen protection. The specific process is as follows: the prepared PANI@MoO_3 nanorods 1.0 g were ultrasonically dispersed in 60 mL of deionized water containing 20 mL of $NH_3 \cdot H_2O$ and the reaction was continuously stirred for 1 h to remove MoO_3. The precipitate was collected by centrifugation and washed several times with deionized water and ethanol, followed by drying at 80°C for 12 h in a vacuum oven. Finally, an amount of the dried sample was placed in a ceramic crucible in the tube furnace under nitrogen protection at a rate of 2°C/min at room temperature to 600°C for 2 h. At the end of the reaction, the samples were finally collected.

Synthesis of Fe_2O_3 modified PANI-derived nitrogen-doped carbon nanotubes

The PNCT obtained from the above preparation was used as a precursor to prepare Fe_2O_3 modified PANI derived nitrogen-doped carbon nanotubes (denoted as Fe_2O_3@PNCT) through hydrothermal and subsequent calcination treatment processes. The process is as follows: 0.135 g of $FeCl_3 \cdot 6H_2O$ and 0.07 g of Na_2SO_4 were ultrasonically dissolved in 50 mL of deionized water with continuous stirring to form a homogeneous solution. Next, 0.015 g of PNCT was added to this mixture and stirred continuously for 20 min to obtain a well-dispersed black suspension. The suspension was then transferred to a 100 mL Teflon-lined stainless-steel autoclave and heated to 160°C at room temperature for 6 h. After the reaction, the sample was washed several times by centrifugation with deionized water and ethanol, and the sample was dried in a vacuum oven at 80°C for 12 h. Finally, several dried samples were placed in a ceramic crucible protected by nitrogen in a tube furnace at a rate of 3°C/min at room temperature to 400°C for 2 h. After the reaction, the brownish red powder samples were collected.

Assembly of quasi-solid-state asymmetric supercapacitors

To demonstrate the electrochemical performance and practical applications of the samples, a quasi-solid state asymmetric supercapacitor was assembled using Ni_2P@PANI hollow nanotubes as the positive electrode, Fe_2O_3@PNCT as the negative electrode, and PVA/KOH gel as the electrolyte. In particular, the preparation of PVA/KOH gel was prepared according to a previous report with slight modifications [2, 25]. The specific process is as follows: 2 g of polyvinyl alcohol (PVA) was dissolved in 40 mL of deionized water and stirred at 130°C until PVA was completely dissolved to form a clear and transparent solution. The solution was cooled to room temperature

with continuous stirring. Next, 10 mL of deionized water containing 2 g of KOH was slowly added to the PVA solution with continuous stirring to form the PVA/KOH gel electrolyte. Subsequently, the positive and negative electrodes were immersed into the PVA/KOH gel for 5 min, and the immersion was repeated three times so that the positive and negative electrode materials were completely coated with gel. Finally, a quasi-solid asymmetric supercapacitor with a sandwich (positive electrode/gel electrolyte/negative electrode) structure can be assembled. In asymmetric SCs, the two electrodes exhibit specific capacitances, masses and potential windows. In order to construct asymmetric SCs, a charge balance relationship, $\boldsymbol{Q}^{+} = \boldsymbol{Q}^{-}$, should be followed between the positive and negative electrodes, where the charge stored by the positive and negative electrodes depends on the specific capacity ($\boldsymbol{C}$), the potential range of the discharge process ($\Delta \boldsymbol{V}$) and the mass of the electrodes ($\boldsymbol{m}$), following the below equation [24, 48]:

$$\boldsymbol{Q}^{+} = \boldsymbol{Q}^{-} \#(1)$$

$$\boldsymbol{Q} = \boldsymbol{C} \times \Delta \boldsymbol{V} \times \boldsymbol{m} \#(2)$$

$$\boldsymbol{C}^{+} \times \Delta \boldsymbol{V}^{+} \times \boldsymbol{m}^{+} = \boldsymbol{C}^{-} \times \Delta \boldsymbol{V}^{-} \times \boldsymbol{m}^{-} \#(3)$$

Thus, calculations based on GCD curves at 2 A g^{-1} showed that the Ni_2P@PANI electrode specific capacity was about 892 C g^{-1} (**Figure 3(c)**), and the specific capacity of Fe_2O_3@PNCT was 328 C g^{-1} (the potential window is 1.0 V, equivalent to 328 F g^{-1}, 91 mA h g^{-1}, in **Figure S23(c)** at 2 A g^{-1}. In this work, the loading mass of active materials was 3.5 ± 0.5 mg for Ni_2P@PANI-2.2 (more details about the mass loading of active material see **Table S4**). From this, it can

be calculated that the load ratio of the positive and negative electrode was approximately 0.61, then the negative electrode Fe_2O_3@PNCT mass loading range was about 6.0 mg and the whole device mass loading was about 10.0 mg.

Material characterization

The morphologies and structures of the samples were characterized by scanning electron microscopy (FE-SEM, JEOL JSM 6700F) and transmission electron microscopy (FEI Tecnai G2 S-Twin F20 D573). The crystal structure of the materials was analyzed by X-ray diffraction (XRD, D/max 2550V/PC, CuKα radiation), and surface elemental analysis. Oxidation states were characterized by X-ray photoelectron spectroscopy (XPS, ESCALAB 250, Mg Kα radiation) and energy dispersive X-ray spectroscopy (EDS, FEI Helios Nanolab 600i), and the specific surface area and pore size distribution results were obtained by specific surface area analyzer (ASAP 2420). The functional groups of the samples were characterized by Fourier transform infrared spectroscopy (Bruker FTIR IFS-66V/S, and pure KBr for spectral backgrounds). The samples were prepared by grinding the resulting powder and KBr in a mortar at a mass ratio of 1:10, followed by pressing at 10 MPa at room temperature to obtain the test samples. Raman spectroscopy was measured in air on a confocal Raman microscope (RM 1000, Renishaw) using a 532 nm laser. All spectral peaks were calibrated against the value of 520.7 cm^{-1} of a silicon wafer.

Electrochemical measurements

Electrochemical measurements were performed on an electrochemical

workstation (CHI760e, CH Instruments Inc., Shanghai) in 2.0 mol L^{-1} KOH. A standard three-electrode system was used, with Ni_2P@PANI or Fe_2O_3@PNCT as the working electrode, Pt foil as the counter electrode, Hg/HgO electrode as the reference electrode. The asymmetric device was investigated using a two-electrode testing cell. The Fe_2O_3@PNCT negative was prepared by grinding a mixture of active material, acetylene black, and PTFE in a mass ratio of 8:1:1, and pressed onto a nickel foam (2 cm × 2 cm) under 3.0 MPa (the positive electrode was prepared in the same way). The average mass loading of Fe_2O_3@PNCT was 4.0 ± 0.5 mg (more details about the mass loading of active material see **Table S4**). Cyclic voltammetry (CV) curves were performed at different scan rates in the potential range of 0.0-0.7 V and –1.0-0.0 V. Galvanostatic charge/discharge (GCD) curves were performed at different current densities in the voltage range 0.0-0.6 V and –1.0-0.0 V. Electrochemical impedance spectroscopy (EIS) was performed at an AC voltage of 5.0 mV amplitude applied in the frequency range 0.01-100 kHz.

The mass specific capacity (C_m), area specific capacity (C_s), energy density (E), and power density (P) of the electrodes and devices are calculated by the following equations [3, 48]:

$$C_{m(C\,g^{-1})} = \frac{i \times \Delta t}{m} \#(4)$$

$$C_{m(Ah\,g^{-1})} = \frac{i \times \Delta t}{3600 \times m} \#(5)$$

$$E = \frac{1}{2} \times C \times \Delta V^2 \#(6)$$

$$P = \frac{E}{\Delta t} \#(7)$$

where C_m (C g^{-1}) is the mass specific capacity, i (A) is the charge/discharge current, Δt (s) is the discharge time, ΔV (V) is the discharge potential window, and m (g) is the electrode active mass loading.

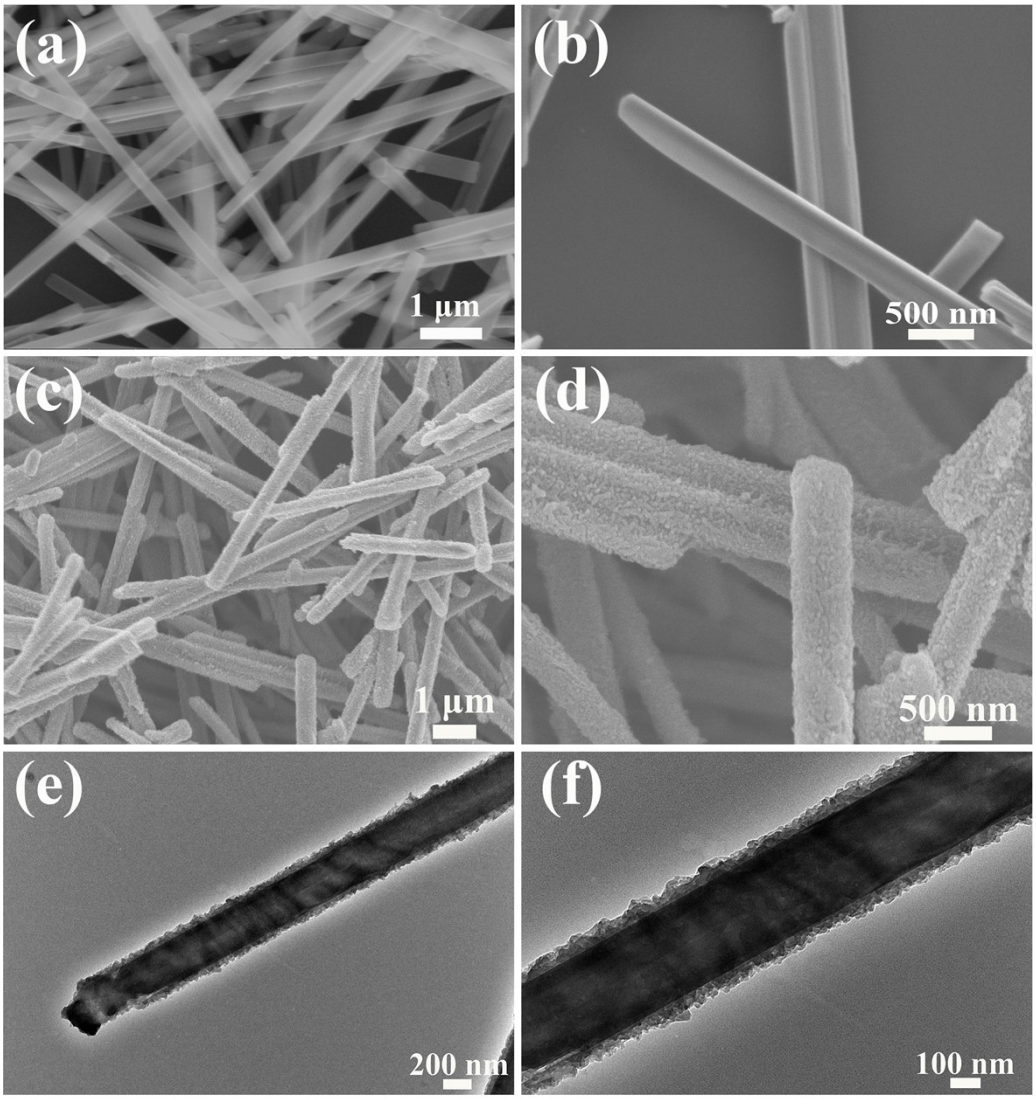

Figure S1: (a, b) SEM images of the MoO_3 template, (c, d) PANI @ MoO_3, and (e, f) the TEM of PANI @ MoO_3.

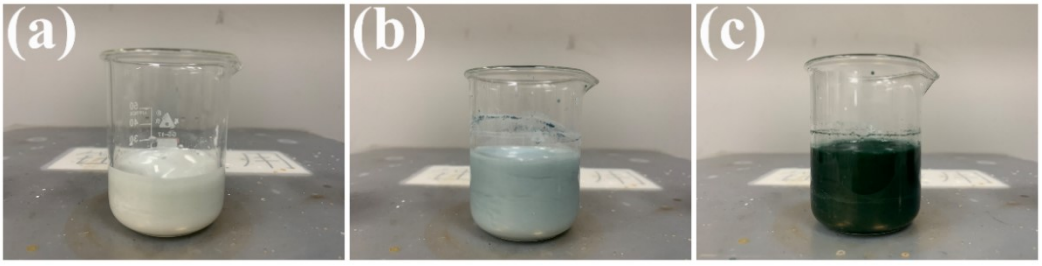

Figure S2: Digital photo image of PANI@MoO_3 sample: (a) 0 minute, (b)30 minutes, and (c) 4 hours.

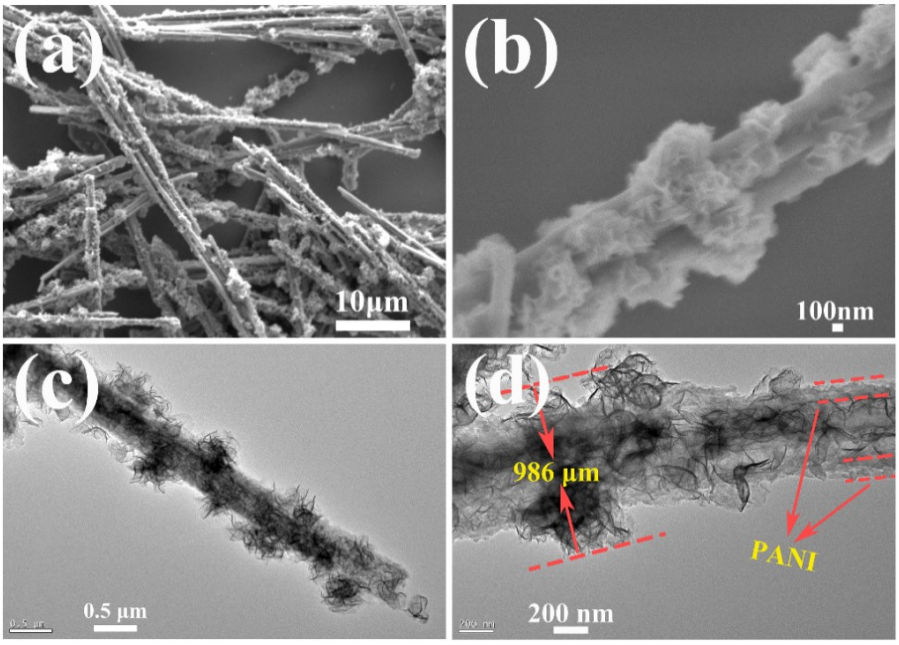

Figure S3: SEM and TEM images of the $Ni(OH)_2$@PANI hollow nanotubes obtained via the CBD reactions under 0.5 mol L^{-1} $NiSO_4$

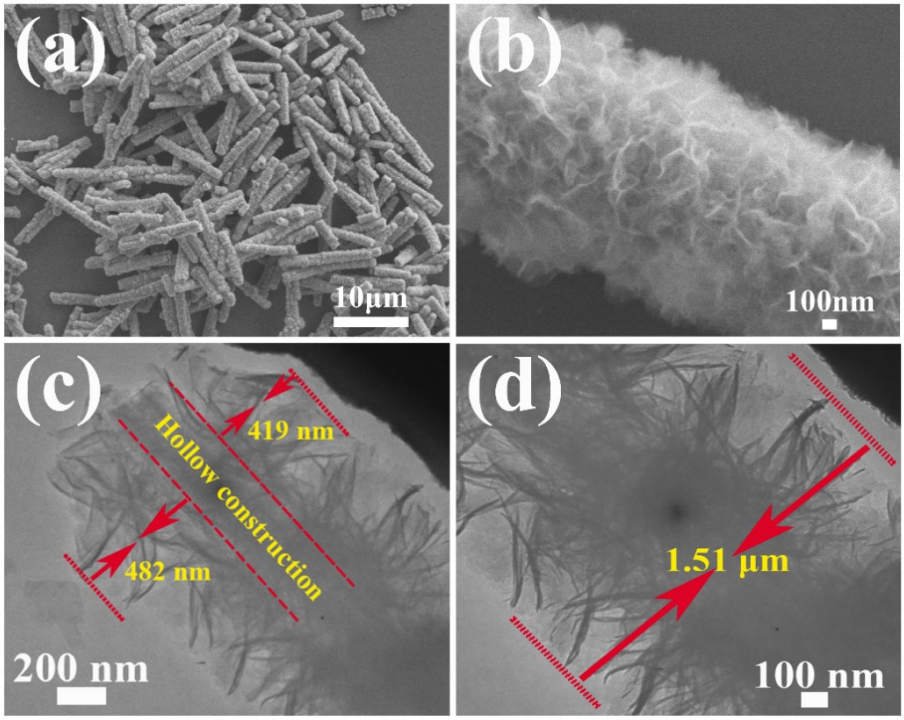

Figure S4: SEM and TEM images of the $Ni(OH)_2$@PANI hollow nanotubes obtained via the CBD reactions under 1.0 mol L^{-1} $NiSO_4$

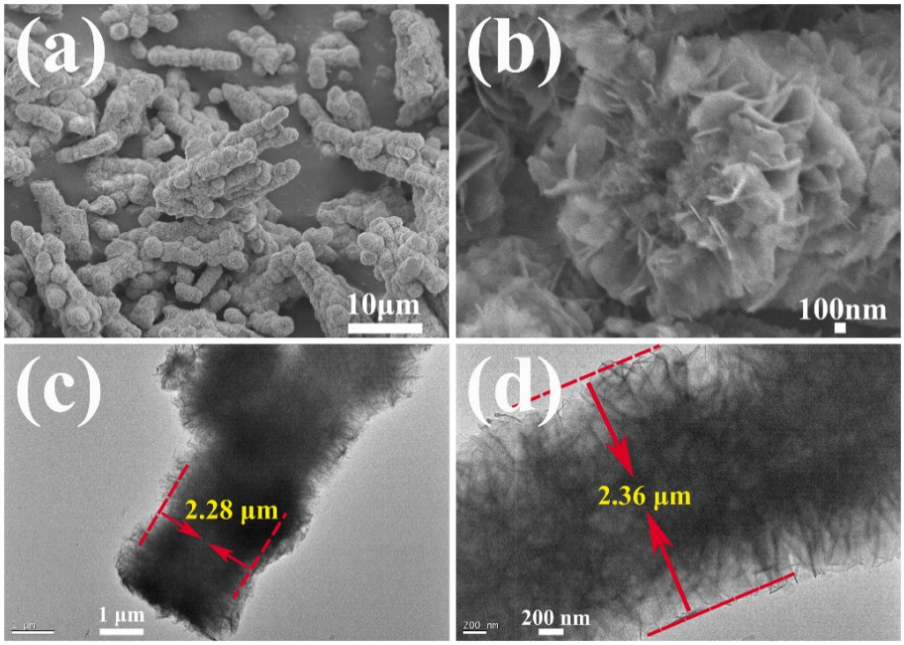

Figure S5: SEM and TEM images of the $Ni(OH)_2$@PANI hollow nanotubes obtained via the CBD reactions under 1.5 mol L^{-1} $NiSO_4$

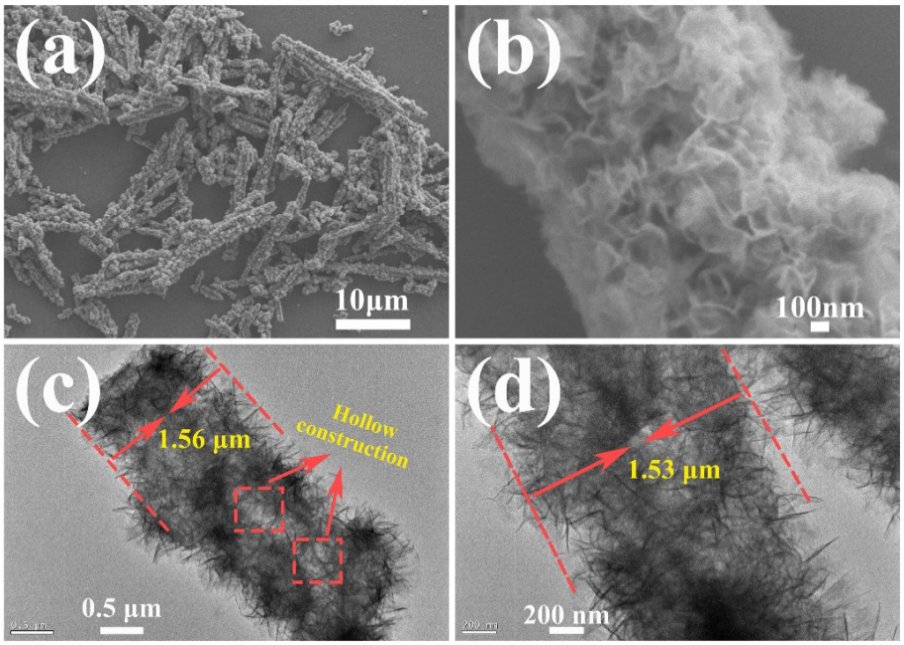

Figure S6: SEM and TEM images of the blank $Ni(OH)_2$ hollow nanotubes obtained via the CBD reactions under 1.0 mol L^{-1} $NiSO_4$ without PANI layer.

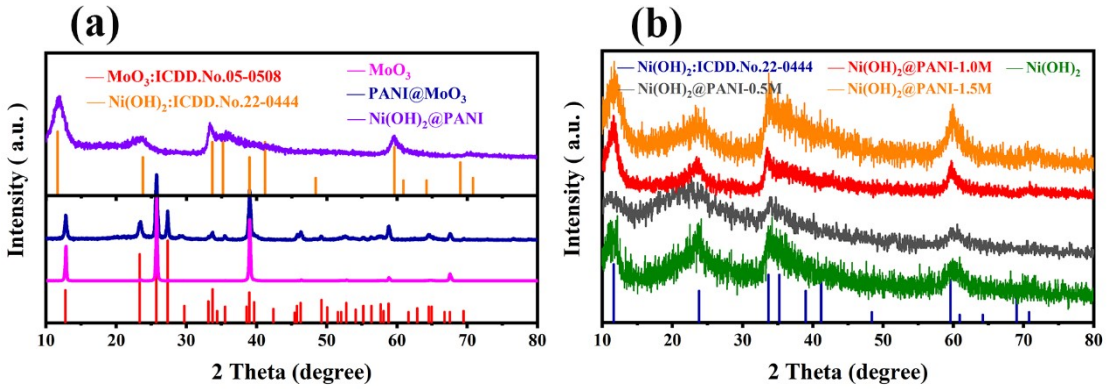

Figure S7: (a) XRD patterns of the MoO_3, PANI@MoO_3, and $Ni(OH)_2$@PANI precursors, (b) XRD patterns of the $Ni(OH)_2$@PANI-x precursors obtained via the CBD reactions at different $NiSO_4$ concentrations

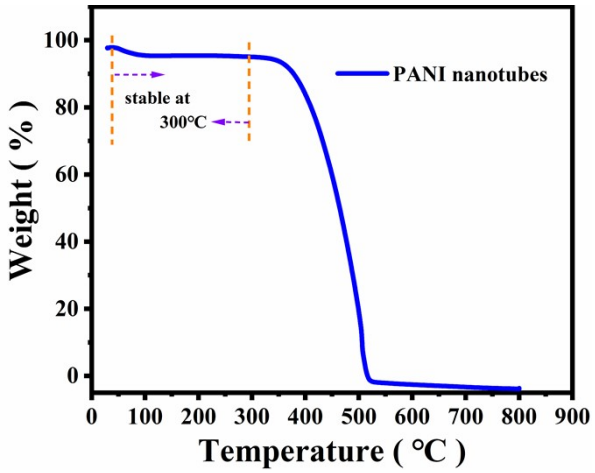

Figure S8: The TGA curves of PANI hollow nanotubes obtained through the removal of MoO_3 template.

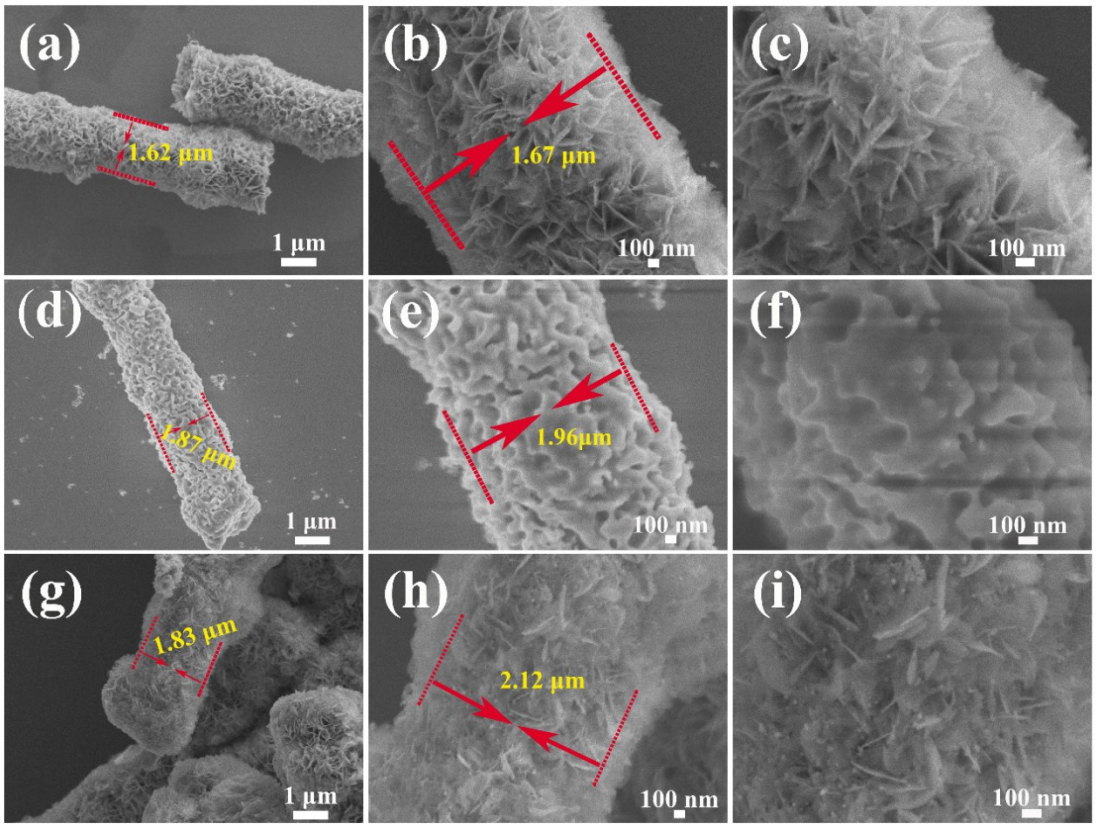

Figure S9: Morphological characterization of different ratios of phosphate samples and the blank samples: (a-c) SEM images of the Ni_2P@PANI-1.2 hollow nanotubes, (d-f) SEM images of the Ni_2P@PANI-3.2 hollow nanotubes, and (g-i) SEM images of the blank Ni_2P hollow nanotubes samples.

At a lower phosphorization ratio of 1.2:1, **Figure S9(a, b)**, due to the low phosphating mass ratio, the reaction rate was slower and thus beneficial to maintain the whole morphological stability, the sample still retained the morphology of the precursor without structural damage. In the high magnification SEM images in **Figure S9(c)**, the smooth surface of $Ni(OH)_2$ nanosheets in PNP-1.2 was transformed into a 'spot-like' particle shape and became rough overall. When the mass ratio was further increased to 3.2:1, as

shown in **Figure S9(d-f)**. The phosphatization at a high mass ratio no longer has uniformly dispersed rough porous nanosheets although the highly ordered nanotube morphology of the precursor was still retained. The excessive reaction destroyed the porous and interconnected Ni_2P sheets, causing the sheets to accumulate on the surface of PANI nanotubes and form a bulk, which no longer has a perfect morphology. For the blank Ni_2P sample, when the phosphatization was carried out with a mass ratio of 2.2:1, the morphology was shown in **Figure S9(g-i)**, and the surface of the nanosheets still formed a rough particle-like morphology with uniform dispersion. Since it did not contain the stable support of PANI nanotubes, the large-scale collapse and fragmentation of the nanosheets with poor morphological retention can be seen in the high magnification images in **Figure S9(h, i)** after the phosphatization process.

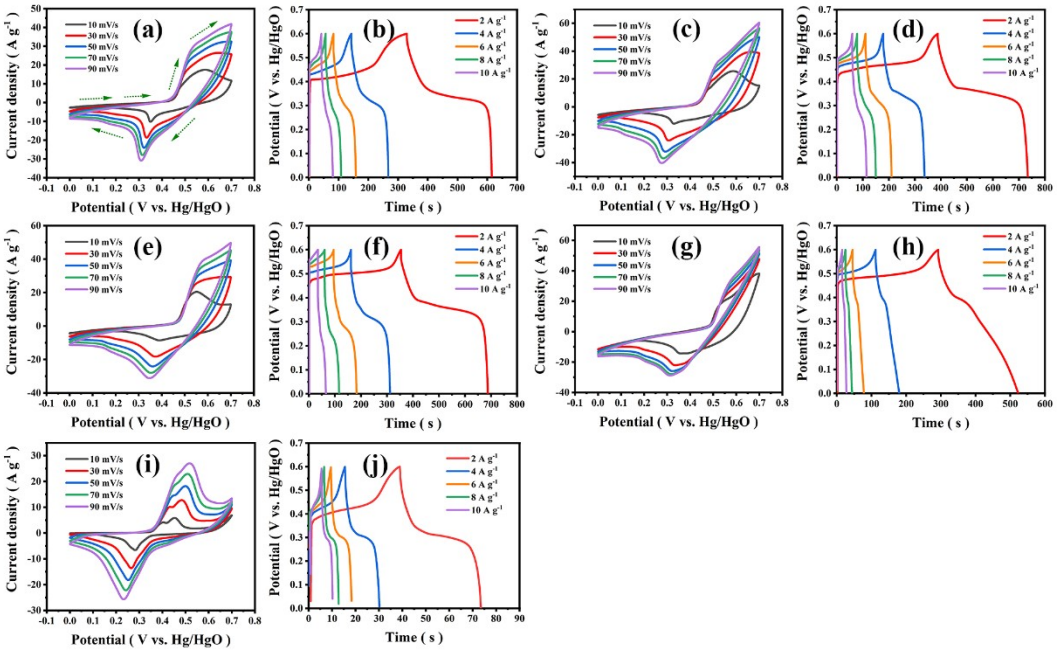

Figure S10：Electrochemical characterization of the CV and GCD curves of $Ni(OH)_2$@PANI-x and blank samples prepared at different $NiSO_4$ concentrations: (a, b) 0.5M, (c, d) 1.0M, (e, f) 1.5M, (g, h) the blank $Ni(OH)_2$ hollow nanotubes, and (i, j) the blank PANI hollow nanotubes samples.

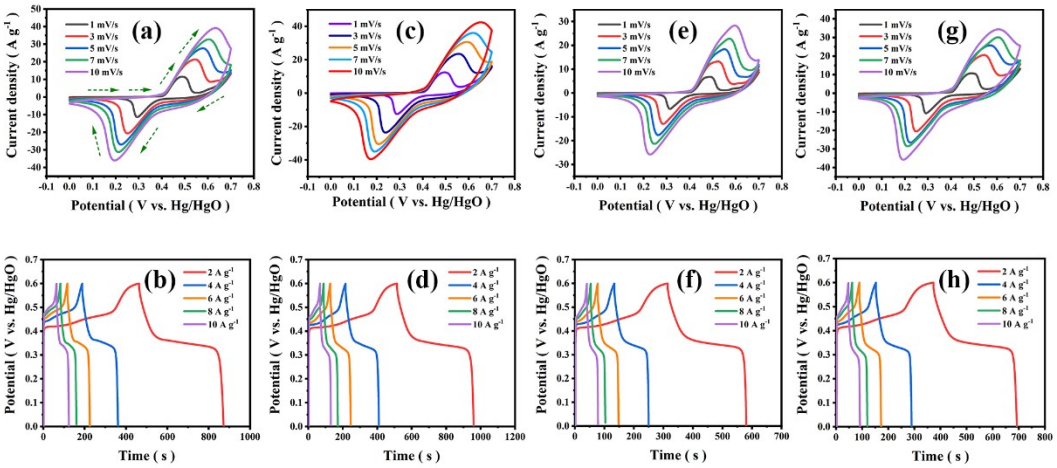

Figure S11: Electrochemical characterization of the CV and GCD curves of Ni_2P@PANI-x and the blank samples prepared at different phosphorization ratios: (a, b)1:1.2, (c, d) 1:2.2, (e, f) 1:3.2, and (g, h) the blank Ni_2P hollow nanotubes samples.

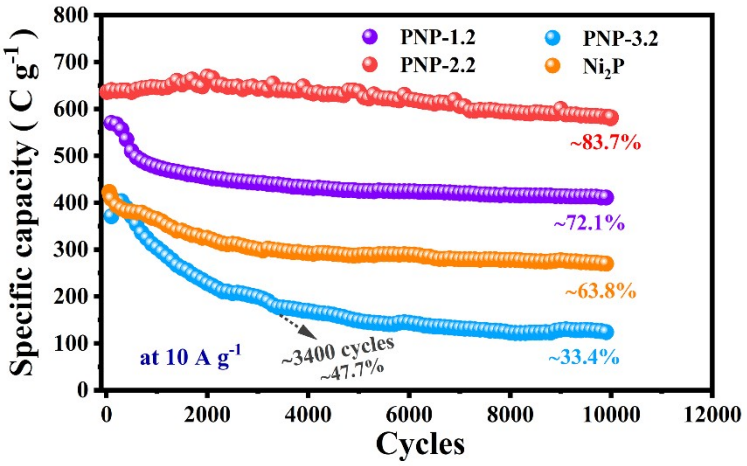

Figure S12: Cycling stability of PNP-x samples measured at a current density of 10 A g^{-1}.

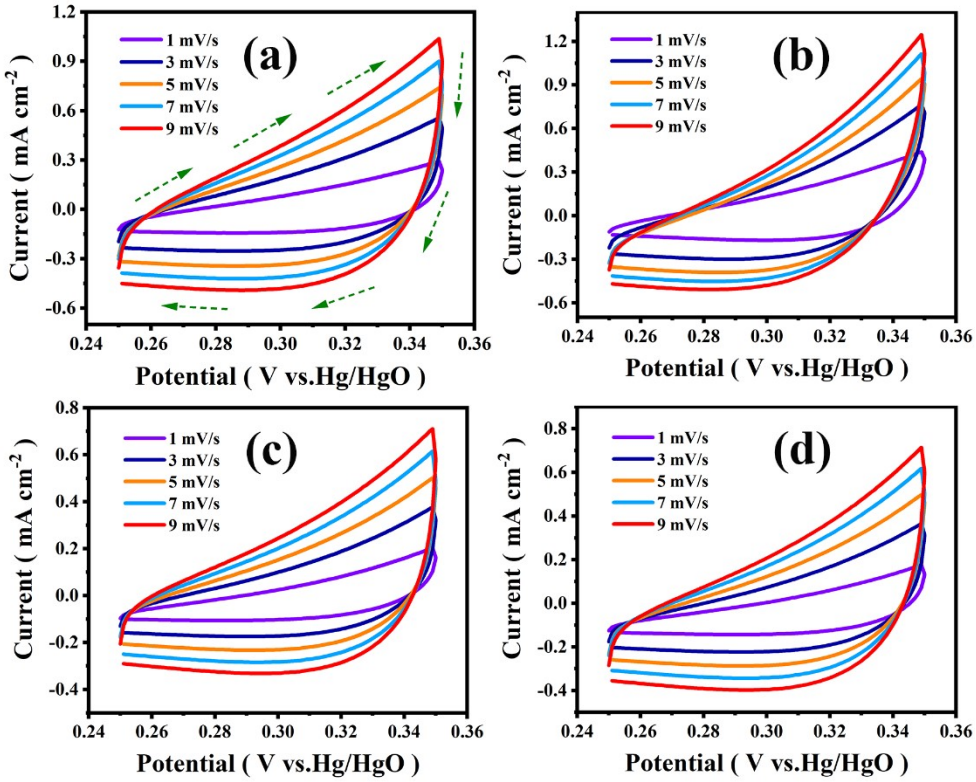

Figure S13: CV curves recorded at different scan rates between 0.25 and 0.35 V for (a) Ni_2P@PANI-1.2, (b) Ni_2P@PANI-2.2, (c) Ni_2P@PANI-3.2, and (d) the blank Ni_2P samples.

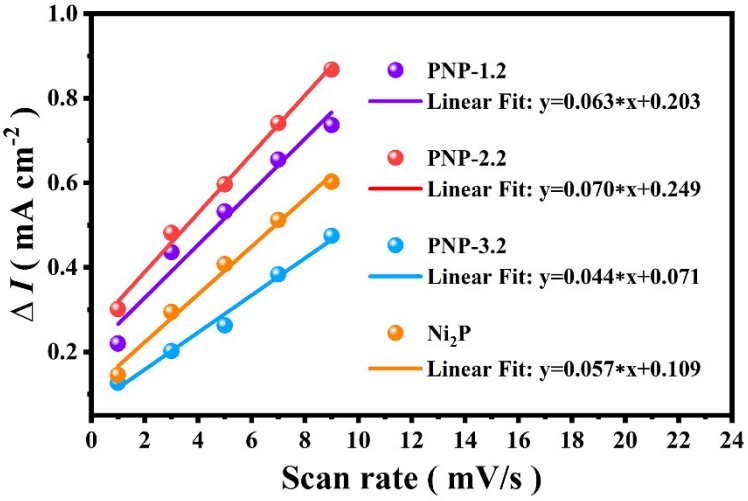

Figure S14: ***ΔI*** measured at 0.30 V vs Hg/HgO plotted as a function of scan rate.

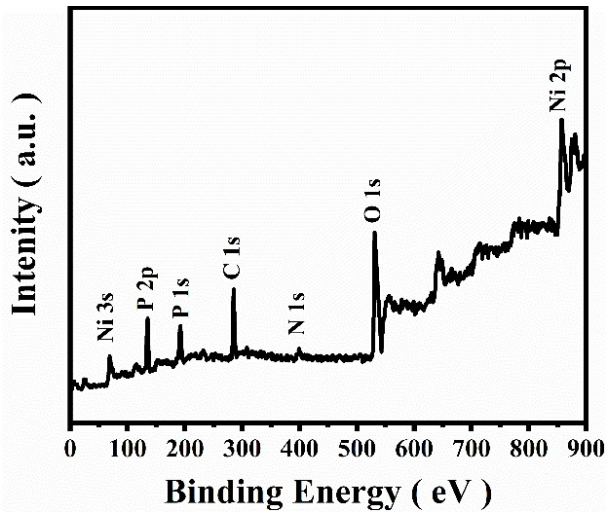

Figure S15: XPS survey spectrum of Ni_2P@PANI hollow nanotubes samples.

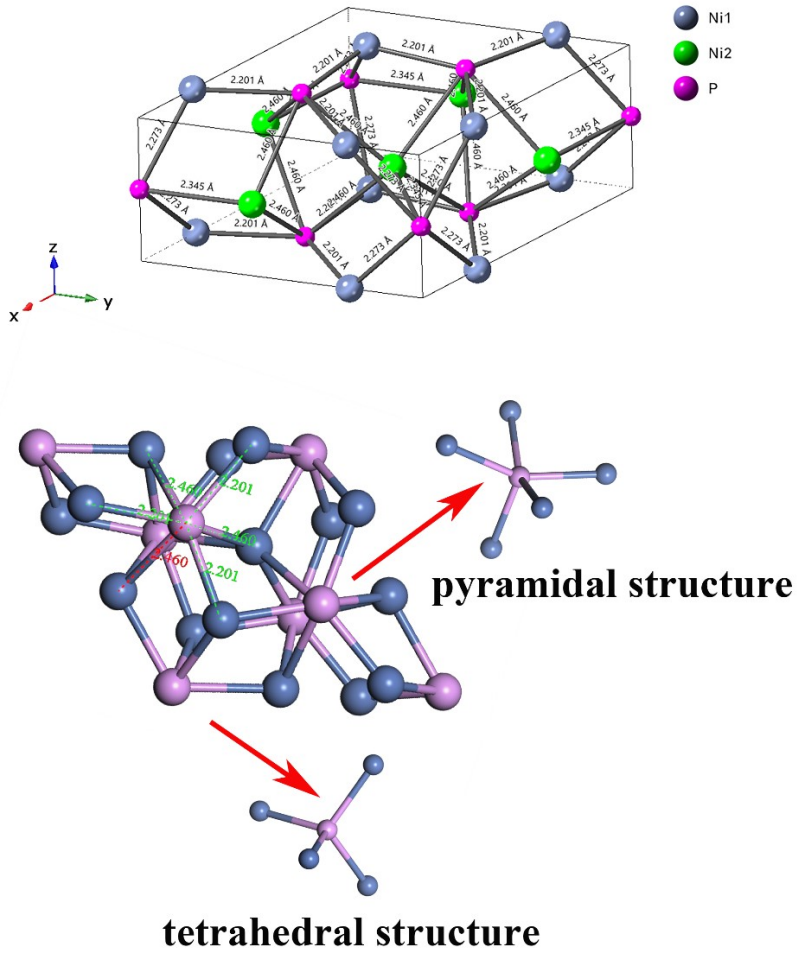

Figure S16: Ni_2P crystal structure unit and its composition.

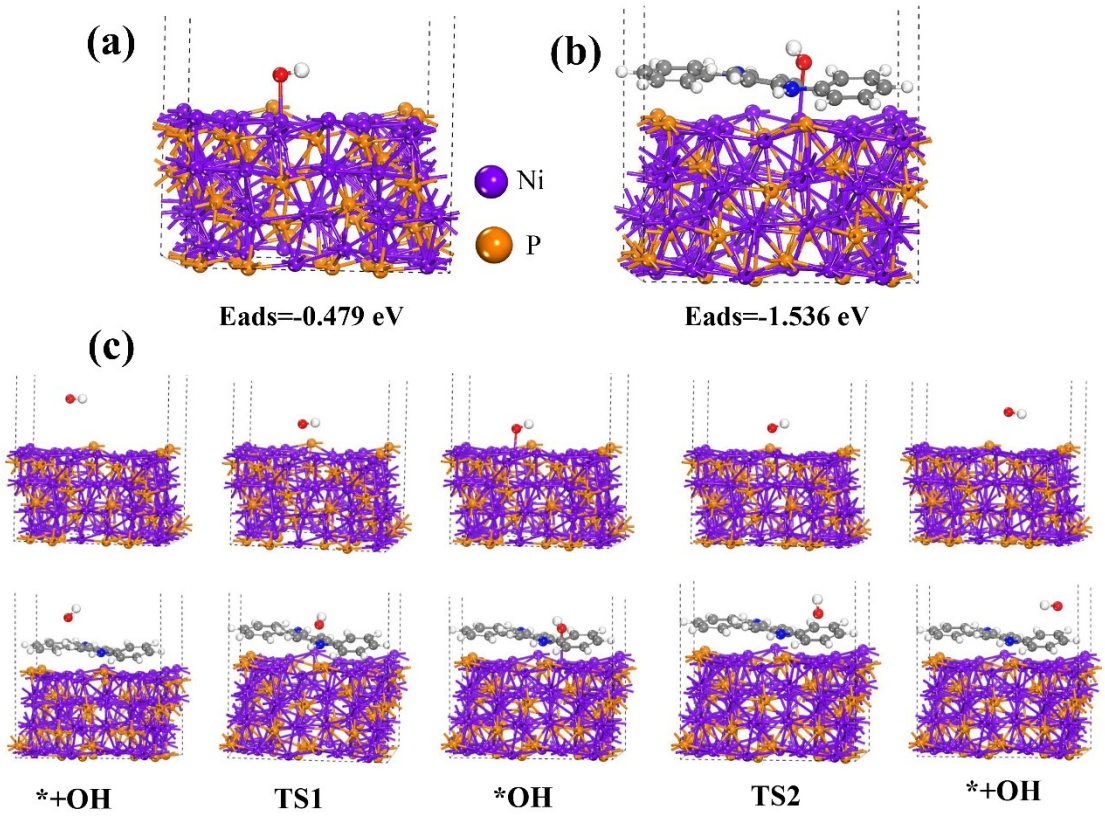

Figure S17: DFT calculations based on the transition state energy of adsorbed hydroxyl (ΔG_{OH^-}): (a) Energy barrier required for stable adsorption of OH^- on blank Ni_2P samples, (b) Energy barrier required for stable adsorption of OH^- on Ni_2P@PANI samples, and (c) the structure of OH^- adsorption and desorption in the structure of the blank Ni_2P and PANI@Ni_2P samples.

Computational methods

We had employed the Vienna Ab Initio Package (VASP) [S2, S3]to perform all the density functional theory (DFT) calculations within the generalized gradient approximation (GGA) using the PBE formulation [S4]. We had chosen the projected augmented wave (PAW) potentials to describe the ionic cores and taken valence electrons into account using a plane wave basis set with a kinetic energy cutoff of 400 eV [S5, S6]. Partial occupancies of the Kohn-Sham orbitals were allowed using the

Gaussian smearing method and a width of 0.05 eV. The electronic energy was considered self-consistent when the energy change was smaller than 10^{-4} eV. A geometry optimization was considered convergent when the force change was smaller than 0.05 eV/Å. The vacuum spacing perpendicular to the plane of the structure is 18 Å. The Brillouin zone integral uses the surfaces structures of 1×1×1 monkhorst pack K point sampling. Finally, the adsorption energies (Eads) are calculated as Eads= Ead/sub -Ead -Esub, where Ead/sub, Ead and Esub are the optimized adsorbate/substrate system, the adsorbate in the structure and the clean substrate respectively. The free energy is calculated as follows:

$$G = E + ZPE - TS \quad (8)$$

where G, E, ZPE and TS are the free energy, total energy from DFT calculations, zero-point energy and entropic contributions, respectively. In our calculation, the U had been employed to calculate the electronic properties, and the 3.68 eV for 3d had been used in our systems.

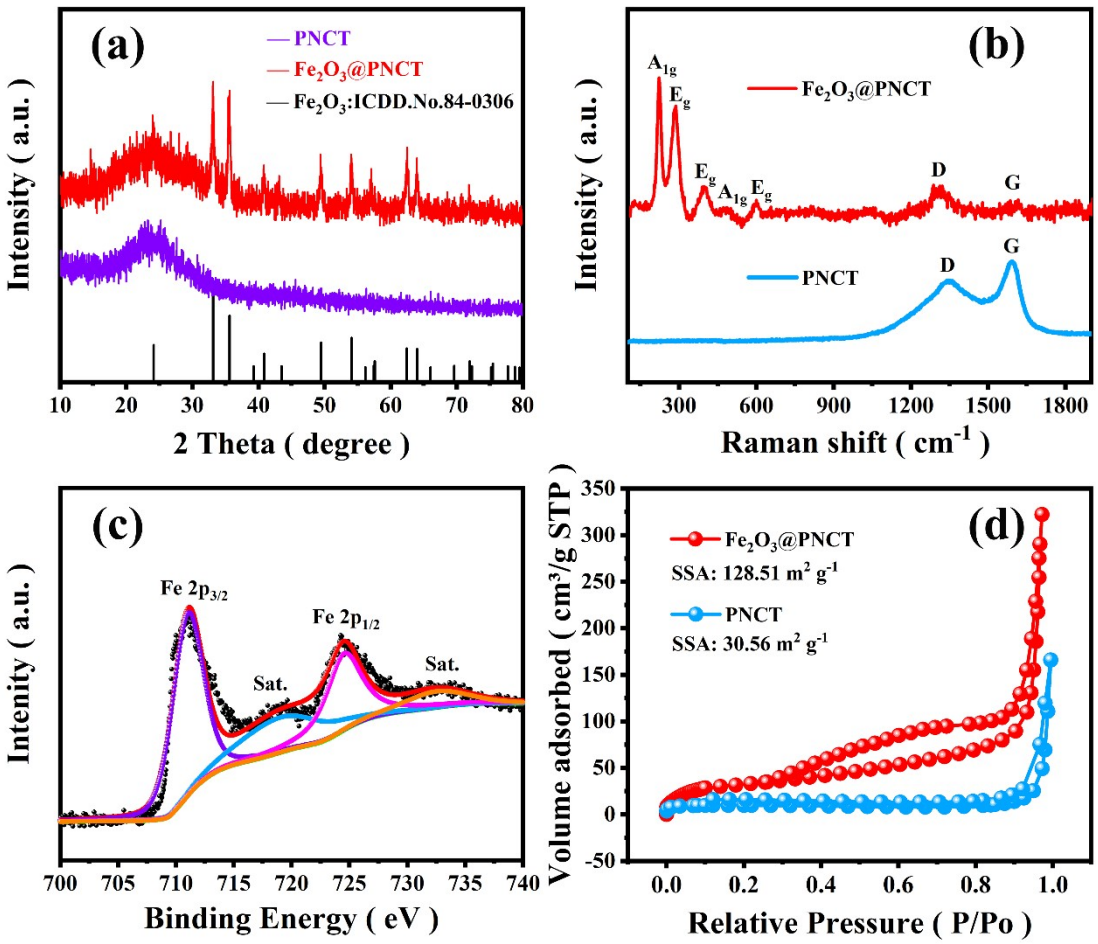

Figure S18: Structural characterization of Fe_2O_3@PNCT samples: (a) XRD patterns, (b) Raman spectrum(powder samples tested at room temperature with a 532 nm laser and calibrated against the value of 520.7 cm^{-1} of a silicon wafer), (c) Fe 2p XPS spectrum, and (d) N_2 adsorption-desorption isotherms.

The phase composition of the product was characterized by XRD, as shown in **Figure S18(a)**. The XRD spectra of Fe_2O_3@PNCT (red spectrum) and PNCT precursor (purple spectrum) both had two relatively broad diffraction peaks at 2θ of ~23.9° and ~43.8°, which were assigned to the graphitic structure of sp^2 hybridization after pyrolytic carbonization. The strong diffraction peaks at the 2θ of 24.2, 33.2, 35.6, 40.8, 49.5, 54.1, 57.4, 62.4, 64.0, 71.9, and 75.5° matched

well with the characteristic diffraction peaks of the rhombohedral phase Fe_2O_3, respectively (ICDD No. 84-0306) [49]. The Raman spectroscopy further characterized the sample structural information, as shown in **Figure S18(b)**. The spectral peaks at ~214.3 and 479.2 cm^{-1} correspond to Fe-O symmetric stretching vibrations (A_{1g} mode), while the peaks near ~277.6, 391.2, and 593.8 cm^{-1} correspond to Fe-O symmetric bending vibrations of Fe_2O_3 (E_g mode), and the peaks at ~1307.8 and 1608.3cm^{-1} correspond to the D and G bands of carbon [S37]. In addition, the chemical composition and valence of the surface of Fe_2O_3@PNCT samples were analyzed by XPS. The survey spectrum of the samples showed the presence of Fe, C, N and O (**Figure S19**). In the high-resolution Fe 2p spectrum, **Figure S18(c)**, the two peaks at ~724.5 and 711.2 eV correspond to the spin-orbit split electrons of Fe $2p_{1/2}$ and Fe $2p_{3/2}$ in Fe_2O_3 [8, S37]. Finally, nitrogen adsorption-desorption tests were conducted for PNCT and Fe_2O_3@PNCT to characterize the pore structure and specific surface area, and the results were shown in **Figure S18(d)** and **Figure S20**. The Fe_2O_3@PNCT had a high specific surface area of 128.51 $m^2 g^{-1}$ and an average pore size distribution of 17.65 nm, which was much larger than that of PNCT at 30.56 $m^2 g^{-1}$ and 8.47 nm. A large specific surface area of Fe_2O_3@PNCT with a rational pore size distribution ensures a fast electron and ion transport, which will contribute to the electrochemical performance of the electrode.

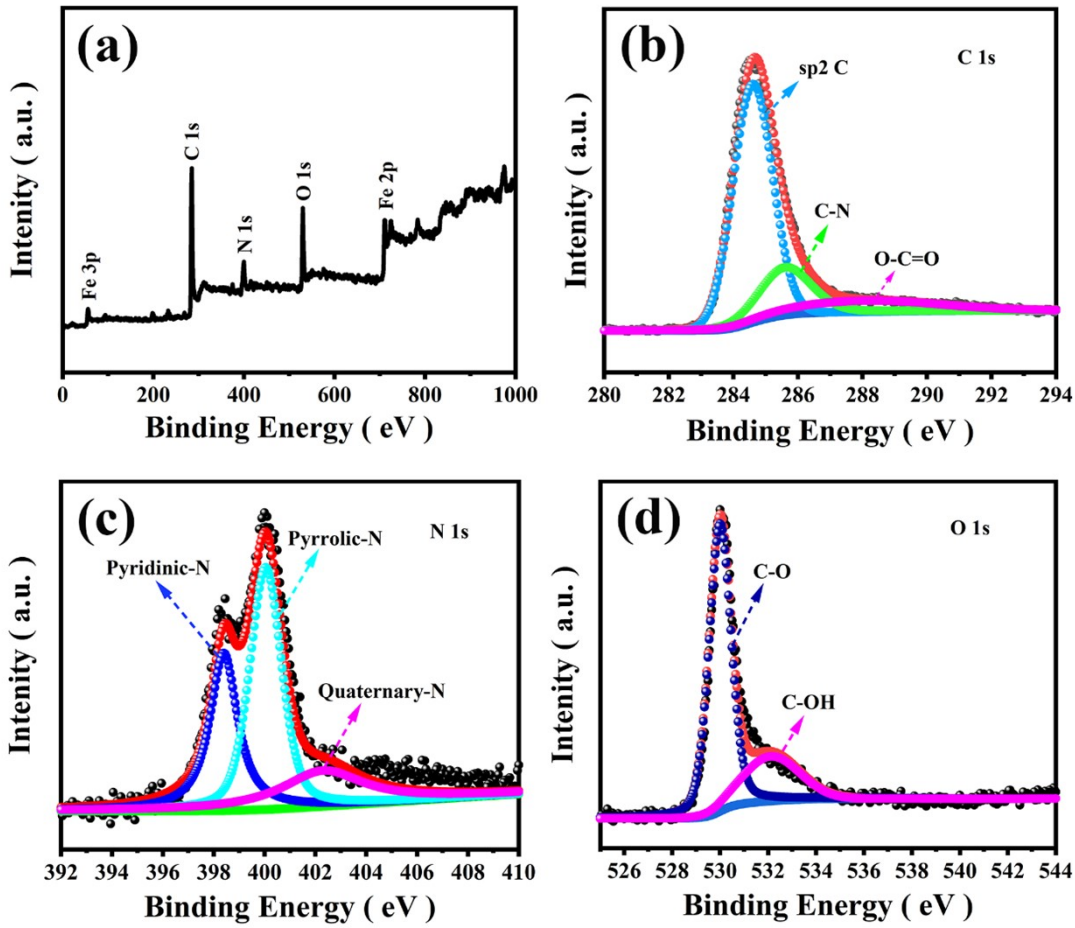

Figure S19: XPS spectrum of Fe_2O_3@PNCT: (a) XPS survey of Fe_2O_3@PNCT, (b) C 1s, (c) N 1s, and (d) O 1s.

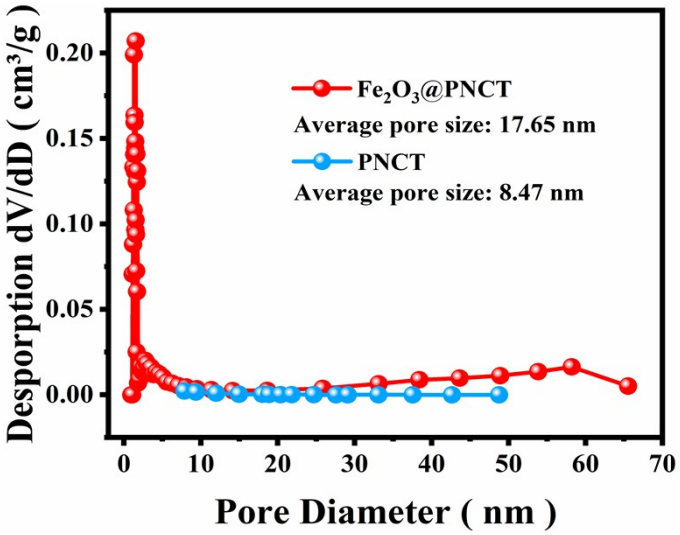

Figure S20: Pore-size distribution curve of Fe_2O_3@PNCT and PNCT samples obtained from the BJH method.

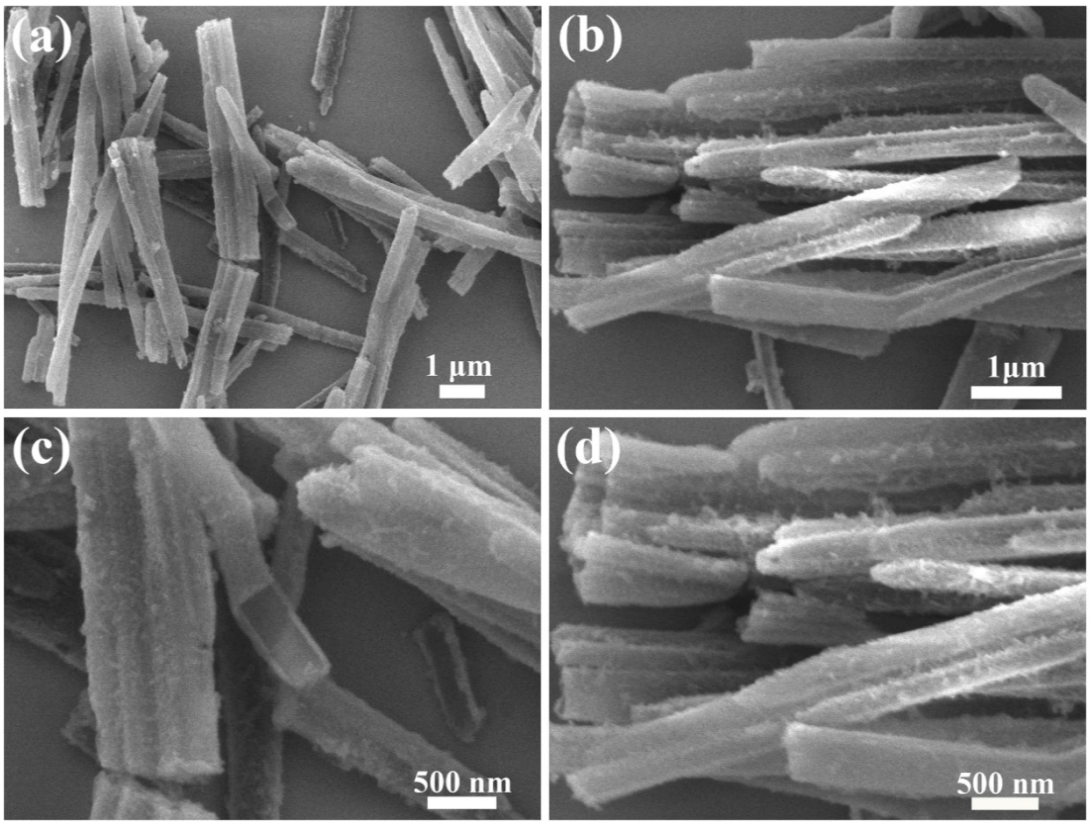

Figure S21: The morphology of PANI nanotubes obtained after the removal of MoO_3 template.

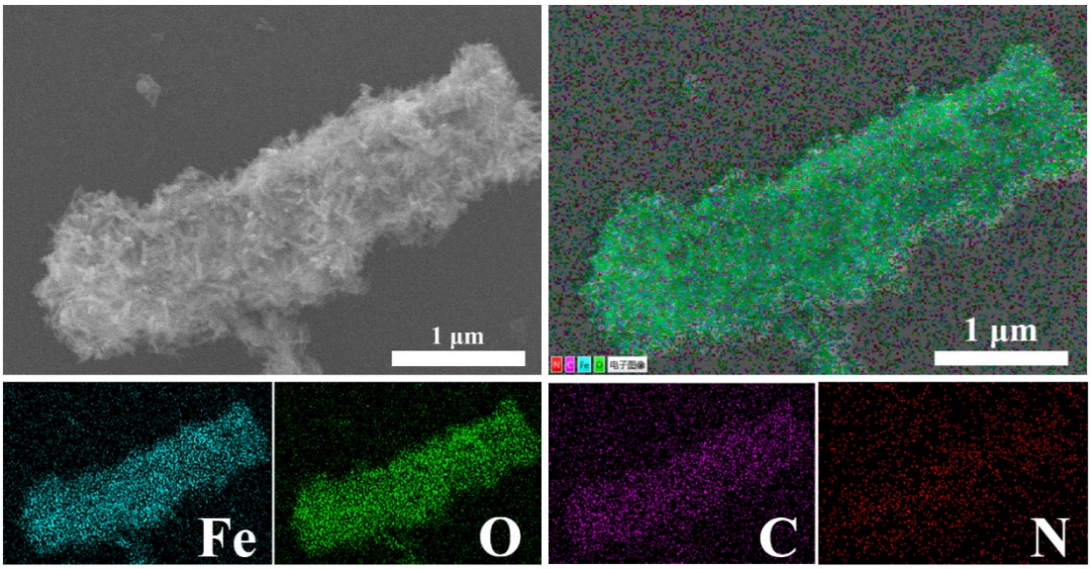

Figure S22: SEM of Fe_2O_3@PNCT and the corresponding elemental mappings of different elements.

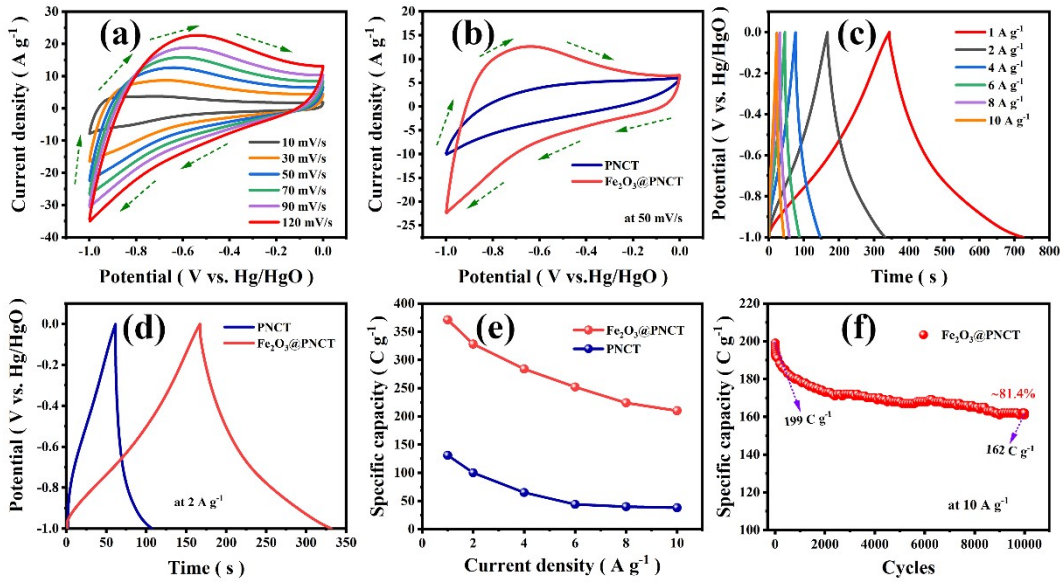

Figure S23: Electrochemical performances of negative electrode: (a) CV curves of the Fe_2O_3@PNCT electrode at various scan rates, (b) comparative CV curves of Fe_2O_3@PNCT at 50 mV s^{-1}, (c) GCD curves of Fe_2O_3@PNCT at different current densities in the range of 1-10 A g^{-1}, (d) comparative GCD curves of PNCT and Fe_2O_3@PNCT samples at 2 A g^{-1}, (e) GCD curves of PNCT and Fe_2O_3@PNCT samples as a function of discharge current density, and (f) cycling stability of Fe_2O_3@PNCT measured at a current density of 10 A g^{-1}.

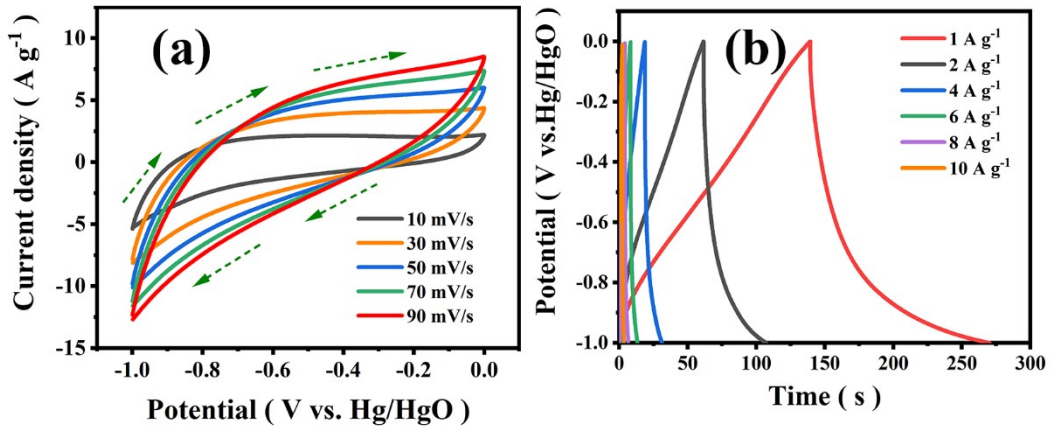

Figure S24: Electrochemical performances of the blank PNCT electrodes: (a) CV curves at various scan rates, and (b) GCD curves at different current densities in the range of 1-10 A g^{-1}.

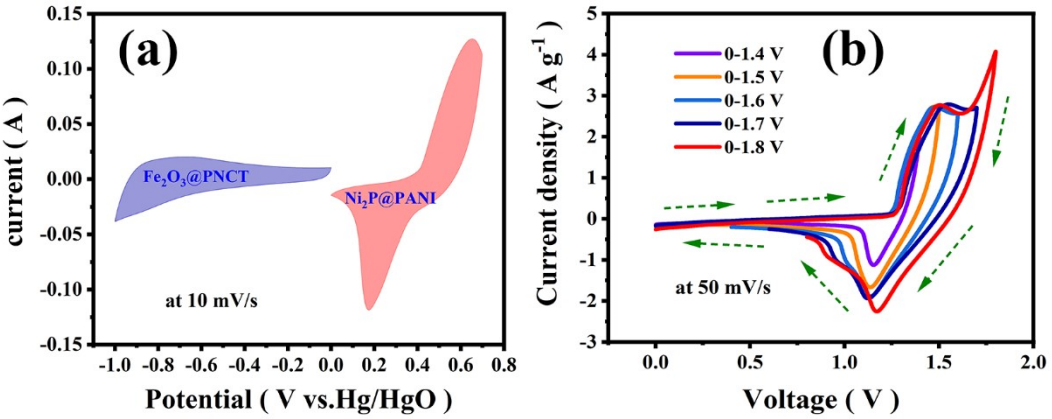

Figure S25: (a) CV curves of Ni_2P@PANI positive electrode and Fe_2O_3@PNCT negative electrode in a three-electrode system at 10 mV s^{-1} after charge balancing, (b) CV curves of the device measured in different voltage ranges.

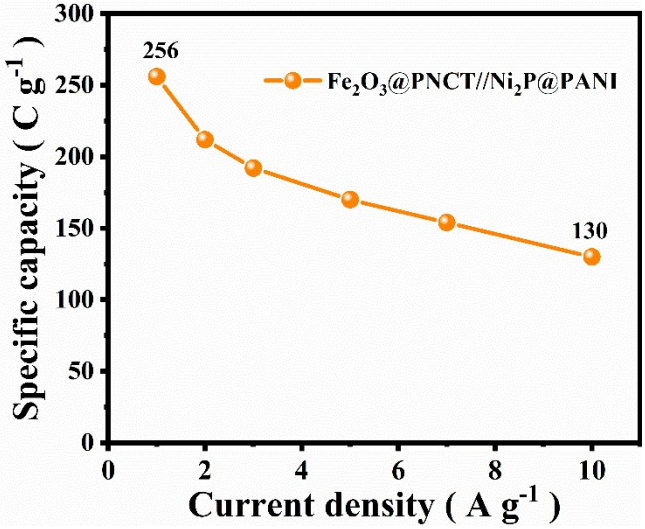

Figure S26: Rate capability of Fe_2O_3@PNCT//Ni_2P@PANI QSSC devices.

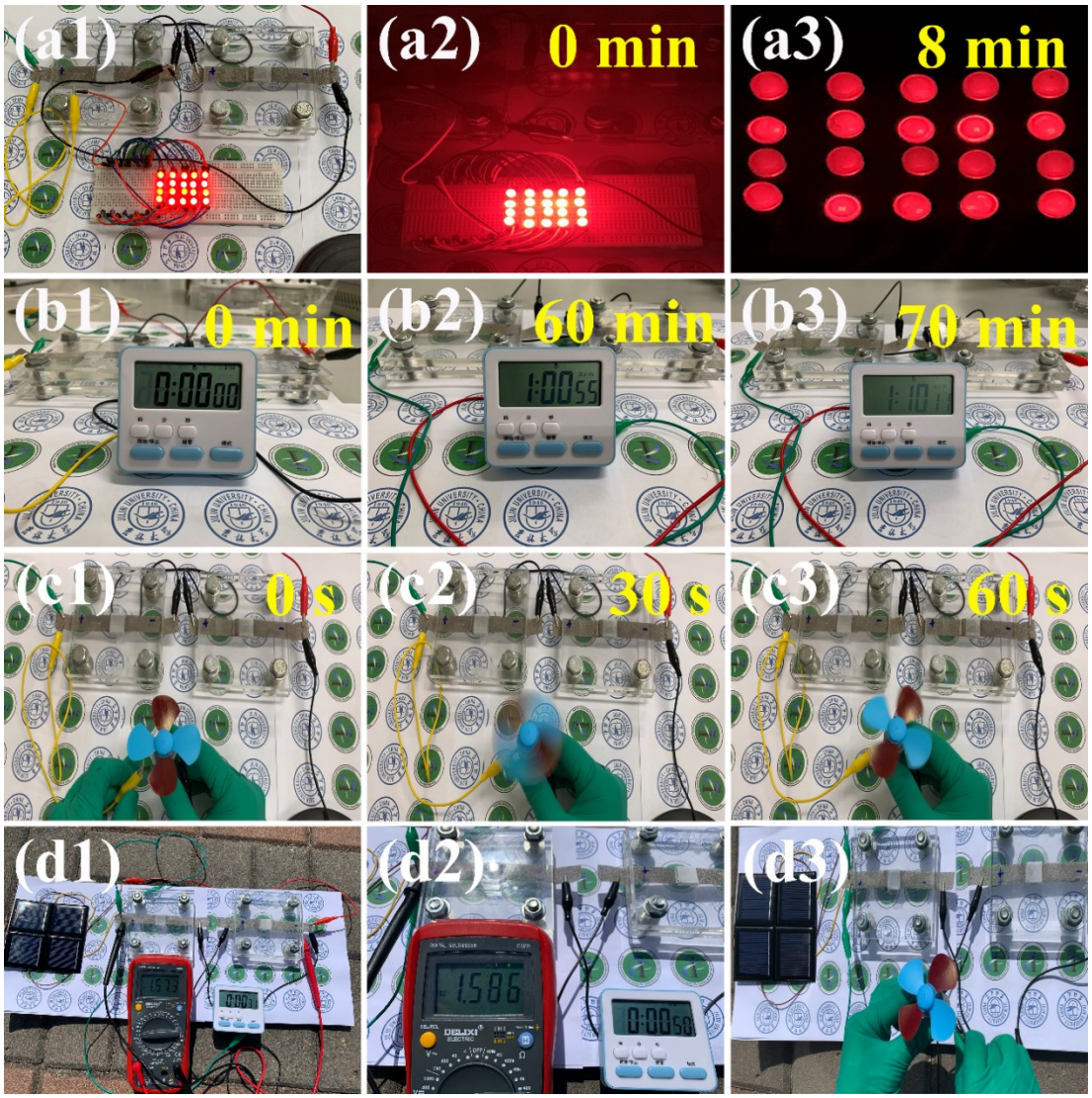

Figure S27: The digital photographs show the practical application of the device: (a1-a3) two devices in series could stably light a light source consisting of 20 red LEDs, (b1-b3) power the alarm clock, (c1-c3) drive a small fan, and (d1-d3) the energy storage and supply system built in combination with commercial solar panels.

Table S1: Comparisons of Ni_2P@PANI electrodes and QSSC devices performance with previous work.

Electrode	Capacity (Current density)	Cell (Config)	Cycles (devices)	Retention (devices)	ΔV (V)	ED (Wh kg^{-1})	Ref.
Ni_2P@PANI hollow nanotube	**866 C g^{-1} 2.0 A g^{-1}**	**2E Fe_2O_3@ PNCT**	**10,000**	**79.8%**	**1.70**	**60.60**	**This work**
Ni_2P NS/NF	1398 C g^{-1} 2.5 A g^{-1}	2E AC	5000	91.3%	1.60	26.00	S7
Ni-P	448 C g^{-1} 2.0 A g^{-1}	2E AC	1000	84.5%	1.60	29.20	S8
Ni_2P/Ni/C	521 C g^{-1} 2.0 A g^{-1}	2E AC	5000	99.0%	1.40	32.02	S9
Ni_2P or Ni_5P_4	337 C g^{-1} 1.0 A g^{-1}	2E Fe_2O_3	1000	96.0%	1.60	35.50	S10
Co_2P nanorod	270 C g^{-1} 2.0 A g^{-1}	2E Graphene	6000	97.0%	1.50	24.00	S11
Cu_3P nanorod	1400 C g^{-1} 2.0 A g^{-1}	2E AC	15,000	65.0%	1.50	76.85	S12
$Ni_{12}P_5$ nanowires	707 C g^{-1} 1.0 A g^{-1}	2E AC	100	~55.0%	1.60	108.20	S13
NiO-GNS/PANI	744 C g^{-1} 2.0 A g^{-1}	2E Sym.	1000	86.0%	0.60	---	S14
$Co_xNi_{1-x}P$/CNF	1405 C g^{-1} 5.0 A g^{-1}	2E AC	10,000	72.0%	1.40	32.20	S15
Ni_xP_y nanosheets	1272 C g^{-1} 2.0 A g^{-1}	2E AC	5000	84.6%	1.50	67.20	S16
Ni-P@NiCo-LDH	1449 C g^{-1} 2.5 A g^{-1}	2E AC	5000	70.0%	1.60	35.10	S17
CoP@NiCoP nanowire	956 C g^{-1} 2.0 A g^{-1}	2E Fe_2O_3	1000	73.3%	1.75	37.16	S18
2D nickel phosphate	176 C g^{-1} 2.0 A g^{-1}	2E AC	5000	100.0%	1.45	50.00	S19
FeNiP@CoNi-LDH	975 C g^{-1} 2.0 A g^{-1}	2E PC	20,000	73.9%	1.60	87.30	S20
NiP@CoAl-LDH	556 C g^{-1} 1.7 A g^{-1}	2E AC	4000	95.5%	1.60	37.18	S21
NiCoP/ NiCo-OH	550 C g^{-1} 1.0 A g^{-1}	2E PC	1000	92.0%	1.60	34.00	S22
Ni-PANI	315 C g^{-1} 2.0 A g^{-1}	3E	5000	~75.0%	---	---	S23

NiCoP@NiCo-LDH	728 C g^{-1} 2.0 A g^{-1}	2E AC	10,000	97.0%	1.70	57.00	S24
NiCoP@NF nanosheet	780 C g^{-1} 2.0 A g^{-1}	2E AC	500	67.2%	1.20	27.00	S25

Note: 3E represents three-electrode systems for single-electrode, **2E** represents two-electrode systems for devices, **AC** represents the activated carbon, **PC** represents the porous carbon, **Sym.** represents the symmetrical devices, and --- represents not mentioned. All values in **Table S1** were recalculated using the standard set of **equation (4)** (as reported in the experimental part) for normalization and more meaningful comparisons.

Table S2: Parameters of the proposed equivalent circuit model.

Electrode	R_s (Ω)	R_{ct} (Ω)	Z_w (Ω)
Ni_2P@PANI-1.2	0.78	7.85	7.18
Ni_2P@PANI-2.2	**0.76**	**5.50**	**6.67**
Ni_2P@PANI-3.2	2.00	16.05	12.09
Ni_2P	0.79	13.19	8.28

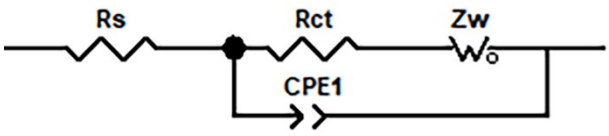

Figure S28: Equivalent Simulation Circuit.

Table S3: Comparisons of Fe_2O_3@PNCT electrodes performance with previous work.

Electrode	Capacity (Current density)	Electrolyte	Cycles (3E)	Retention (3E)	ΔV (V)	Ref.
Fe_2O_3@PNCT	**371 C g^{-1} 1 A g^{-1}**	**2 M KOH**	**10,000**	**81.4%**	**1.0**	**This work**
FeOCl	278 C g^{-1} 0.8 A g^{-1}	1 M Na_2SO_4	10,000	75.0%	1.0	S26
g-C_3N_4/α-Fe_2O_3	260 F g^{-1} 0.5 A g^{-1}	2.5 M Li_2SO_4	1000	100.0%	1.0	S27
SiC@Fe_2O_3	721 F g^{-1} 2.0 A g^{-1}	2 M KOH	---	---	1.2	S28
α-Fe_2O_3/C	345 F g^{-1} 1.8 A g^{-1}	1 M Na_2SO_4	4000	91.8%	1.0	S29
N doped graphene/Fe_2O_3	260 F g^{-1} 2.0 A g^{-1}	1 M Na_2SO_4	1000	82.5%	1.2	S30
Fe_2O_3/N-CNT	264 F g^{-1} 1.0 A g^{-1}	2 M KOH	10,000	84.0%	1.0	S31
α-Fe_2O_3/rGO	270 F g^{-1} 1.0 A g^{-1}	1 M Na_2SO_4	5000	123.0%	1.5	S32
Fe_7S_8/α-FeOOH	520 F g^{-1} 1.0 A g^{-1}	1 M KOH	5000	90.6%	1.1	S33
PANI@Fe_3O_4@CF	245 F g^{-1} 0.5 A g^{-1}	1 M H_2SO_4	10,000	82.4%	0.65	S34
FeS_2 nano-ellipsoids	515 C g^{-1} 1.0 A g^{-1}	2 M KOH	5000	88%	1.1	S35
NS-Fe_3O_4@N-PC	866 F g^{-1} 1.0 A g^{-1}	1 M KOH	5000	78.2%	0.4	S36

Note: 3E represents three-electrode systems for single-electrode and the values of ΔV in **Table S3** are all obtained from the discharge voltage range in the GCD curves in the cited reference.

Table S4: The mass loading of active material in three-electrode system for all samples.

Electrode	M_{total} (mg cm^{-2})	Percentage (%)	M_{active} (mg cm^{-2})	Average
	4.56		3.65	
$Ni(OH)_2$@PANI-0.5M	4.71	8:1:1	3.77	3.5 ± 0.5
	4.12		3.29	
	5.11		**4.08**	
$Ni(OH)_2$@PANI-1.0M	**5.63**	**8:1:1**	**4.50**	**4.0 ± 0.5**
	4.43		**3.54**	
	4.27		3.42	
$Ni(OH)_2$@PANI-1.5M	4.61	8:1:1	3.69	3.4 ± 0.5
	4.83		3.86	
	5.03		4.02	
$Ni(OH)_2$	4.08	8:1:1	3.26	3.5 ± 0.5
	4.52		3.62	
	3.92		3.14	
Ni_2P@PANI-1.2	4.64	8:1:1	3.71	3.6 ± 0.5
	5.22		4.18	
	4.39		**3.51**	
Ni_2P@PANI-2.2	**5.10**	**8:1:1**	**4.08**	**3.5 ± 0.5**
	4.13		**3.30**	
	5.20		4.16	
Ni_2P@PANI-3.2	6.35	8:1:1	5.08	4.5 ± 0.5
	5.82		4.66	
	3.63		2.90	
Ni_2P	3.52	8:1:1	2.82	2.8 ± 0.5
	4.10		3.28	
	4.44		**3.55**	
Fe_2O_3@PNCT	**5.03**	**8:1:1**	**4.02**	**4.0 ± 0.5**
	5.64		**4.51**	
	4.66		3.72	
PNCT	4.25	8:1:1	3.40	3.5 ± 0.5
	4.90		3.92	

Note: M_{total} represents the total mass of the electrode material (2 cm × 2 cm), including the PTFE and acetylene black, **Percentage** represents the active material, acetylene

black, and PTFE in a mass ratio of 8:1:1, **M $_{active}$** represents the active material available on the actual electrode (2 cm × 2 cm), and the **Average** represents the mass loading range of the active material on the electrode (Since there is no guarantee that the operation is exactly the same during each electrode preparation, the mass loading deviation of each sample cannot be avoided. As such, an average specific capacity is more appropriate in this paper).

Table S5: The average specific capacity of the electrode under optimal phosphatization conditions.

Electrode	M $_{total}$ (mg cm^{-2})	Percentage (%)	M $_{active}$ (mg cm^{-2})	Capacity (C g^{-1})	Average (C g^{-1})
Ni_2P@PANI-2.2	4.39	8:1:1	3.51	892	**~866**
	5.10	8:1:1	4.08	753	
	4.13	8:1:1	3.30	952	

Note: The electrode test was performed at 2 A g^{-1}.

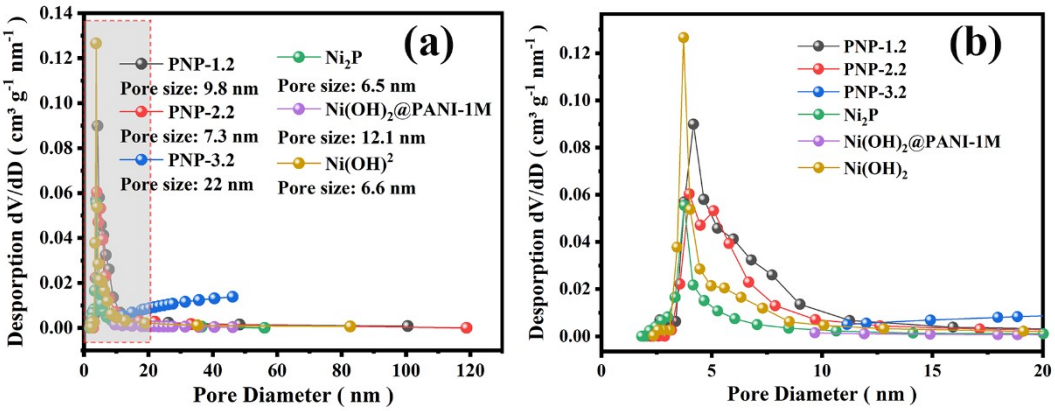

Figure S29: Pore-size distribution curve of PNP-x and precursor samples obtained from the BJH method (note that the data are average pore sizes).

References

[S1] Ma, F. X.; Wu, H. B.; Xia, B. Y.; Xu, C. Y.; Lou, X. W., Hierarchical ß-Mo_2C Nanotubes Organized by Ultrathin Nanosheets as a Highly Efficient Electrocatalyst for Hydrogen Production, *Angew. Chem., Int. Ed.* **2015,** *54* (51), 15395-9.

[S2] Kresse, G.; Furthmuller, J., Efficient iterative schemes for ab initio total-energy calculations using a plane-wave basis set, *Phys. Rev. B Condens Matter.***1996,** *54* (16), 11169-11186.

[S3] Perdew, J. P.; Burke, K.; Ernzerhof, M., Generalized Gradient Approximation Made Simple, *Phys. Rev. Lett.* **1996,** *77* (18), 3865-3868.

[S4] Kresse, G.; Joubert, D., From ultrasoft pseudopotentials to the projector augmented-wave method, *Phys. Rev. B* **1999,** *59* (3), 1758-1775.

[S5] Blochl, P. E., Projector augmented-wave method, *Phys. Rev. B Condens Matter.* **1994,** *50* (24), 17953-17979.

[S6] Grimme, S.; Antony, J.; Ehrlich, S.; Krieg, H., A consistent and accurate ab initio parametrization of density functional dispersion correction (DFT-D) for the 94 elements H-Pu, *J. Chem. Phys.* **2010,** *132* (15), 154104.

[S7] Zhou, K.; Zhou, W.; Tang, Z.; Li, L.; Chen, S., Ultrahigh-Performance Pseudocapacitor Electrodes Based on Transition Metal Phosphide Nanosheets Array via Phosphorization: A General and Effective Approach, *Adv. Funct. Mater.* **2015,** *25* (48), 7530-7538.

[S8] Wang, D.; Kong, L.-B.; Liu, M.-C.; Zhang, W.-B.; Luo, Y.-C.; Kang, L., Amorphous NieP materials for high performance pseudocapacitors, *J. Power Sources* **2015,** *274*, 1107-1113.

[S9] Hou, S. J.; Xu, X. T.; Wang, M.; Xu, Y. Q.; Lu, T.; Yao, Y. F.; Pan, L. K., Carbon-incorporated Janus-type Ni_2P/Ni hollow spheres for high performance hybrid supercapacitors, *J. Mater. Chem. A* **2017,** *5* (36), 19054-19061.

[S10]Wang, D.; Kong, L. B.; Liu, M. C.; Luo, Y. C.; Kang, L., An Approach to Preparing Ni-P with Different Phasesfor Use as SupercapacitorElectrode Materials, *Chem. Eur. J.* **2015,** *21* (49), 17897-17903.

[S11]Chen, X.; Cheng, M.; Chen, D.; Wang, R., Shape-Controlled Synthesis of Co_2P Nanostructures and Their Application in Supercapacitors, *ACS Appl. Mater. Interfaces* **2016,** *8* (6), 3892-3900.

[S12]Chodankar, N. R.; Shinde, P. A.; Patil, S. J.; Hwang, S. K.; Raju, G. S. R.; Ranjith, K. S.; Dubal, D. P.; Huh, Y. S.; Han, Y. K., Solution-free self-assembled growth of ordered tricopper phosphide for efficient and stable hybrid supercapacitor, *Energy Storage Mater.* **2021,** *39*, 194-202.

[S13]Gan, Y.; Wang, C.; Chen, X.; Liang, P.; Wan, H. Z.; Liu, X.; Tan, Q. Y.; Wu, H.; Rao, H.; Wang, H. B.; Zhang, J.; Wang, Y.; van Aken, P. A.; Wang, H., High conductivity $Ni_{12}P_5$ nanowires as high-rate electrode material for battery-supercapacitor hybrid devices, *Chem. Eng. J.* **2020,** *392*.

[S14]Wu, X. M.; Wang, Q. G.; Zhang, W. Z.; Wang, Y.; Chen, W. X., Nano nickel oxide coated graphene/polyaniline composite film with high electrochemical performance for flexible supercapacitor, *Electrochim. Acta* **2016,** *211*, 1066-1075.

[S15]Zhang, N.; Li, Y.; Xu, J.; Li, J.; Wei, B.; Ding, Y.; Amorim, I.; Thomas, R.; Thalluri, S. M.; Liu, Y.; Yu, G.; Liu, L., High-Performance Flexible Solid-State Asymmetric Supercapacitors Based on Bimetallic Transition Metal Phosphide Nanocrystals, *ACS Nano* **2019,** *13* (9), 10612-10621.

[S16]Liu, S.; Sankar, K. V.; Kundu, A.; Ma, M.; Kwon, J. Y.; Jun, S. C., Honeycomb-Like Interconnected Network of Nickel Phosphide Heteronanoparticles with Superior Electrochemical Performance for Supercapacitors, *ACS Appl. Mater. Interfaces* **2017,** *9* (26), 21829-21838.

[S17]Xing, J.; Du, J.; Zhang, X.; Shao, Y.; Zhang, T.; Xu, C., A Ni-P@NiCo LDH core-shell nanorod-decorated nickel foam with enhanced areal specific capacitance for high-performance supercapacitors, *Dalton Trans.* **2017,** *46* (30), 10064-10072.

[S18]Wang, X.; Jing, C.; Zhang, W. Z.; Wang, X. S.; Liu, X. Y.; Dong, B. Q.; Zhang, Y. X., One-step phosphorization synthesis of CoP@NiCoP nanowire/nanosheet composites hybrid arrays on Ni foam for high-performance supercapacitors, *Appl. Surf. Sci.* **2020,** *532*.

[S19]Wulan Septiani, N. L.; Kaneti, Y. V.; Fathoni, K. B.; Wang, J.; Ide, Y.; Yuliarto, B.; Nugraha; Dipojono, H. K.; Nanjundan, A. K.; Golberg, D.; Bando, Y.; Yamauchi, Y., Self-assembly of nickel phosphate-based nanotubes into two-dimensional crumpled sheet-like architectures for high-performance asymmetric supercapacitors, *Nano Energy* **2020,** *67*.

[S20]Wan, L.; Chen, D. Q.; Liu, J. X.; Zhang, Y.; Chen, J.; Xie, M. J.; Du, C., Construction of FeNiP@CoNi-layered double hydroxide hybrid nanosheets on carbon cloth for high energy asymmetric supercapacitors, *J. Power Sources* **2020,** *465*.

[S21]Wang, S. L.; Huang, Z. C.; Li, R.; Zheng, X.; Lu, F. X.; He, T. B., Template-assisted synthesis of NiP@CoAl-LDH nanotube arrays with superior electrochemical performance for supercapacitors, *Electrochim. Acta* **2016,** *204*, 160-168.

[S22]Li, X.; Wu, H. J.; Elshahawy, A. M.; Wang, L.; Pennycook, S. J.; Guan, C.; Wang, J., Cactus-Like NiCoP/NiCo-OH 3D Architecture with Tunable Composition for High-Performance Electrochemical Capacitors, *Adv. Funct. Mater.* **2018,** *28* (20).

[S23]Inamdar, A. I.; Chavan, H. S.; Kim, H.; Im, H., Mesoporous Ni-PANI composite electrode for electrochromic energy storage applications, *Sol. Energy Mater. Sol. Cells* **2019,** *201*.

[S24]Gao, X. Y.; Zhao, Y. F.; Dai, K. Q.; Wang, J. T.; Zhang, B.; Shen, X. J., NiCoP nanowire@NiCo-layered double hydroxides nanosheet heterostructure for flexible asymmetric supercapacitors, *Chem. Eng. J.* **2020,** *384*.

[S25]Lan, Y.; Zhao, H.; Zong, Y.; Li, X.; Sun, Y.; Feng, J.; Wang, Y.; Zheng, X.; Du, Y., Phosphorization boosts the capacitance of mixed metal nanosheet arrays for high performance supercapacitor electrodes, *Nanoscale* **2018,** *10* (25), 11775-11781.

[S26]Wan, C. C.; Jiao, Y.; Bao, W. H.; Gao, H.; Wu, Y. Q.; Li, J., Self-stacked multilayer FeOCl supported on a cellulose-derived carbon aerogel: a new and high-performance anode material for supercapacitors, *J. Mater. Chem. A* **2019,** *7* (16), 9556-9564.

[S27]Xu, L.; Xia, J.; Xu, H.; Yin, S.; Wang, K.; Huang, L.; Wang, L.; Li, H., Reactable ionic liquid assisted solvothermal synthesis of graphite-like C_3N_4 hybridized α-Fe_2O_3 hollow microspheres with enhanced supercapacitive performance, *J.Power Sources* **2014,** *245*, 866-874.

[S28]Zhao, J.; Li, Z. J.; Yuan, X. C.; Yang, Z.; Zhang, M.; Meng, A.; Li, Q. D., A High-Energy Density Asymmetric Supercapacitor Based on Fe_2O_3 Nanoneedle Arrays and $NiCo_2O_4$/$Ni(OH)_2$ Hybrid Nanosheet Arrays Grown on SiC Nanowire Networks as Free-Standing Advanced Electrodes, *Adv. Energy Mater.* **2018,** *8* (12).

[S29]Chen, D.; Zhou, S.; Quan, H.; Zou, R.; Gao, W.; Luo, X.; Guo, L., Tetsubo-like α-Fe_2O_3/C nanoarrays on carbon cloth as negative electrode for high-performance asymmetric supercapacitors, *Chem. Eng. J.* **2018,** *341*, 102-111.

[S30]Zhao, P. H.; Li, W. L.; Wang, G.; Yu, B. Z.; Li, X. J.; Bai, J. T.; Ren, Z. Y., Facile hydrothermal fabrication of nitrogen-doped graphene/Fe_2O_3 composites as high performance electrode materials for supercapacitor, *J. Alloys Comp.* **2014,** *604*, 87-93.

[S31]Gnana Sundara Raj, B.; Ko, T. H.; Acharya, J.; Seo, M.-K.; Khil, M.-S.; Kim, H.-Y.; Kim, B.-S., A novel Fe_2O_3-decorated N-doped CNT porous composites derived from tubular polypyrrole with excellent rate capability and cycle stability as advanced supercapacitor anode materials, *Electrochim. Acta* **2020,** *334*.

[S32]Sajjad, M.; Lu, W., Regulating high specific capacitance NCS/α-MnO_2 cathode and a wide potential window α-Fe_2O_3/rGO anode for the construction of 2.7 V for high performance aqueous asymmetric supercapacitors, *J.Energy Storage* **2021,** *44*,103343.

[S33]Zhang, D.; Kong, X.; Zhang, F.; Lei, X., Electric-Field-Assisted Enhanced Electron Transfer to Boost Supercapacitor Negative Electrode Performance for a Fabricated Fe_7S_8/α-FeOOH Nano-Heterostructure, *Adv. Electron. Mater.* **2020,** *6*, 1900953.

[S34]Movassagh-Alanagh, F.; Bordbar-Khiabani, A.; Ahangari-Asl, A., Fabrication of a ternary PANI@Fe_3O_4@CFs nanocomposite as a high performance electrode for

solid-state supercapacitors, *Int. J. Hydrogen Energy* **2019,** *44* (49), 26794-26806.

[S35]Sun, Z. Q.; Yang, X.; Lin, H. M.; Zhang, F.; Wang, Q.; Qu, F. Y., Bifunctional iron disulfide nanoellipsoids for high energy density supercapacitor and electrocatalytic oxygen evolution applications, *Inorg. Chem. Front.* **2019,** *6* (3), 659-670.

[S36]Zhu, M.; Chen, Q.; Tang, J.; Wei, W.; Li, S., Core@shell β-FeOOH@polypyrolle derived N, S-codoped Fe_3O_4@N-doped porous carbon nanococoons for high performance supercapacitors, *Appl. Surf. Sci.* **2019,** *480*, 582-592.

[S37] Wang, Y. D.; Shen, C.; Niu, L. Y.; Li, R. Z.; Guo, H. T.; Shi, Y. X.; Li, C.; Liu, X. J.; Gong, Y. Y., Hydrothermal synthesis of $CuCo_2O_4$/CuO nanowire arrays and RGO/Fe_2O_3 composites for high-performance aqueous asymmetric supercapacitors, *J. Mater. Chem. A* **2016,** 4 (25), 9977-9985.